Supplementary Materials

S1 Station Information

Table S1. Station Information

Expedition	Time	Region	Stations
Healy 0702	2007/05/18-2007/06/16	Bering Sea	92
3rd CHINARE	2008/07/23-2008/07/27	Bering Sea	20
6th CHINARE	2014/07/28-2014/08/13	Chukchi Sea	29
Araon 2011	2011/08/02-2011/08/16	Chukchi borderland	18
Araon 2015	2015/08/05-2015/08/20	Chukchi borderland	22
Sino-Russian 2016	2016/08/28-2016/09/16	East Siberian Sea, Chukchi Sea	30
Sino-Russian 2018	2018/09/22-2018/10/10	Laptev Sea, East Siberian Sea	29

S2 Correction of Chl-*a* concentration

Water samples were collected during all expeditions except the 2018 Sino-Russian cruise. For each sample, 250-500 mL was filtered using GF/F glass fiber filters (Gelman), which were then frozen for subsequent laboratory analysis. The extraction was performed using 90% acetone, following the procedure outlined by Welschmeyer [75]. After storage at 4°C for one day, the samples were centrifuged, and Chl-*a* concentrations were subsequently measured using a fluorometer calibrated against certified Chl-*a* standards. For the ALEC-CTD sensor, calibrations were conducted using the Chl-*a* concentrations obtained from these water samples. The calibration curves are displayed in Figure S1, with adjustments for the Sino-Russian 2018 expedition based on data collected from all other summer expeditions, as illustrated in Figure S1E& F. Additionally, the calibration results for the data from the Araon-2011 and -2015 expeditions are detailed in Zhu et al. [76].

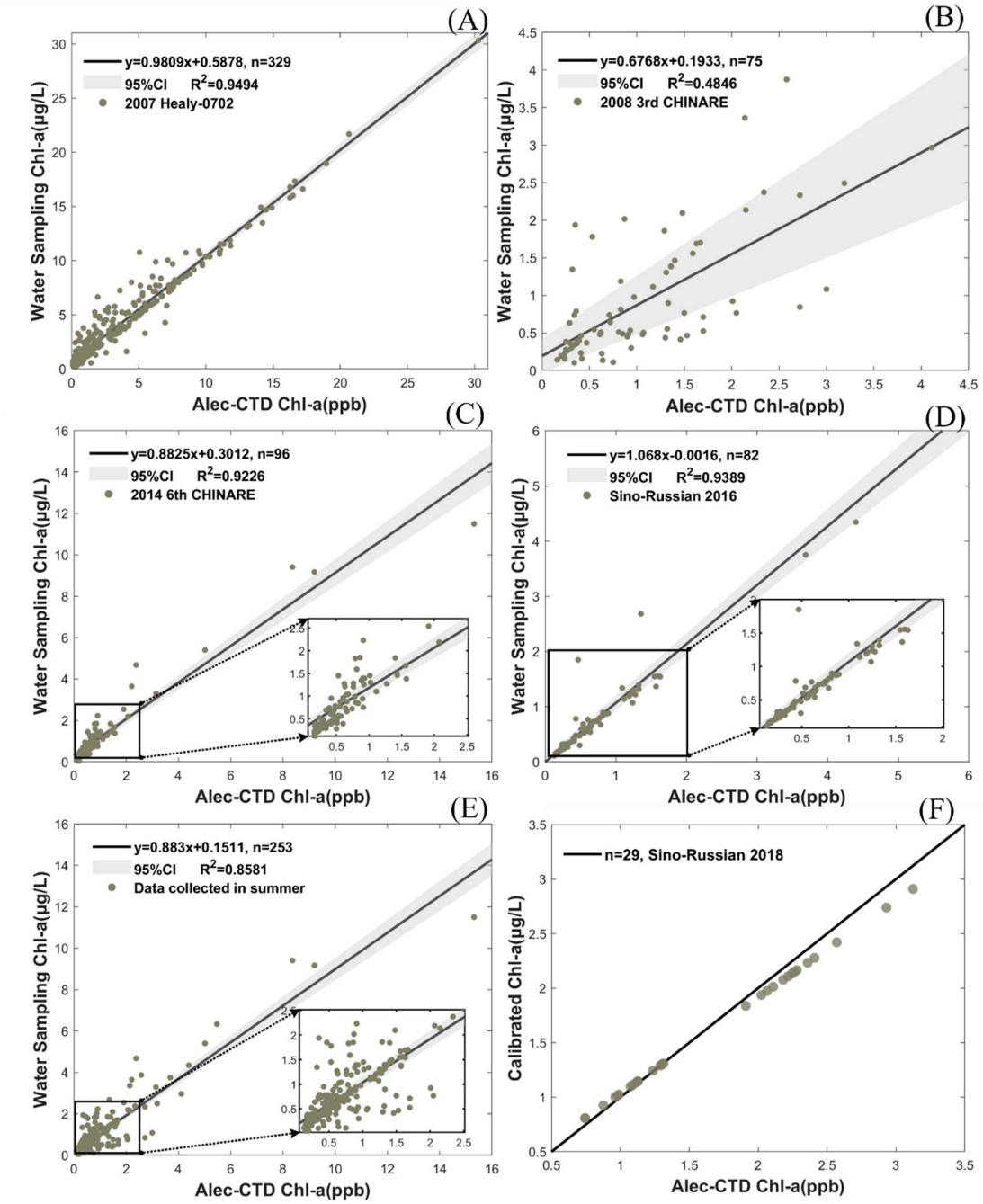


Figure S1: Calibration of ALEC-CTD Sensor Chl-*a* Measurements. Scatter plots compare the Chl-*a* concentrations measured by the ALEC-CTD sensor against those derived from water samples. Data are shown from the Healy-0702 expedition (A), the 3rd CHINARE (B), the 6th CHINARE (C), and the Sino-Russian 2016 expedition (D). The calibration curve based on aggregated summer data, excluding the Laptev Sea, is displayed (E). The curve from (E) is applied to correct Chl-*a* measurements from the Sino-Russian 2018 expedition (F).

S3 Improvement of NIR Algorithms

As shown in Table S2, optimized algorithm parameters using observational data can significantly improve performance, reducing the RMSE to below 1.65, a notable

improvement compared to the evaluation result (RMSE II > 8.16). Among them, the two-band algorithms, RVI and NDVI, demonstrate a higher R^2 (0.69 to 0.73), with RMSE < 1.43. Apart from the MCI algorithm fitted in the POL form (R^2 = 0.71, RMSE = 1.42) within the three-band algorithms, the R^2 for other forms remain < 0.66, overall performing less effectively than the two-band algorithms. Finally, by comparing three empirical models (L, POW, POL) in terms of R^2 and RMSE, the results of the POL fitting are closer to the measured values.

Table S2. The optimized parameters of NIR algorithms.

Algorithm	Formula	R^2	RMSE
Meris-Two band	$11.18R_{rs}(\lambda_2)/\ R_{rs}(\lambda_1)$-1.815	0.70	1.43
Meris-Three band	$117.2(R_{rs}(\lambda_1)^{-1}$-$R_{rs}(\lambda_2)^{-1})\ R_{rs}(\lambda_3)$+9.263	0.61	1.62
DVI-L	21910Dvi+9.226	0.64	1.55
DVI-POW	$(15470\text{Dvi} + 7.206)^{1.124}$	0.63	1.55
DVI-POL	-8457000Dvi^2+21140Dvi+9.278	0.64	1.58
RVI-L	11.18Rvi-1.815	0.70	1.43
RVI-POW	$(7.834\text{Rvi} - 0.538)^{1.124}$	0.69	1.43
RVI-POL	-14.95Rvi^2+38.41Rvi-13.7	0.73	1.37
NDVI-L	20.29Dvi+9.516	0.72	1.37
NDVI-POW	$(14.31\text{Ndvi} + 7.409)^{1.124}$	0.70	1.38
NDVI-POL	-26.68Ndvi^2+16.6Ndvi+9.678	0.73	1.37
TBM-L	117.2Tbm+9.263	0.61	1.62
TBM-POW	$(82.73\text{Tbm} + 7.234)^{1.124}$	0.59	1.62
TBM-POL	-303.1Tbm^2+111.8Tbm+9.321	0.61	1.65
MCI-L	20680Mci+5.108	0.66	1.50
MCI-POW	$(14390\text{Mci} + 4.333)^{1.124}$	0.66	1.51
MCI-POL	-53980000Mci^2+40040Mci+3.934	0.71	1.42

During the fitting with the POW function, the power index was fixed at 1.124. In fact, setting the power index to vary within the positive range has minimal impact on the fitted R^2.

S4 Evaluation of a $K_d(490)$ model derived from $L_w(\lambda)$

Wang and Son et al. [77] proposed a model for estimating $K_d(490)$ based on $L_w(\lambda)$, using data collected from the Chesapeake Bay, USA. The algorithm is defined as follows:

$$K_d(490) = \frac{2.697\times10^{-4}}{R(488)} + 1.045\frac{R(667)}{R(488)} + 4.18[7\times10^{-4} + 2.7135R(667)]\times\{1 - 0.52\exp[-\frac{2.533\times10^{-3}}{R(488)} - 9.817\frac{R(667)}{R(488)}]\}, \quad \text{(S1)}$$

and $R(\lambda)$ can be computed from $nL_{\mathrm{w}}(\lambda)$ as Loisel and Morel (2001):

$$R(\lambda) = \frac{4nL_{\mathrm{w}}(\lambda)}{0.52F_0(\lambda)+1.7nL_{\mathrm{w}}(\lambda)}, \quad \text{(S2)}$$

where $F_0(\lambda)$ is the standard extraterrestrial solar irradiance at wavelength λ, with values of 179.5 and 139.0 for 488 nm and 667 nm, respectively. As illustrated in Figure S2, the algorithm exhibits acceptable performance only under low-attenuation conditions, specifically when $K_{\mathrm{d}}(490) < 0.25\ m^{-1}$. In general, it substantially overestimates $K_{\mathrm{d}}(490)$, yielding an average value of $0.41 \pm 1.91\ m^{-1}$, with an RMSE of 1.88 and a MAPE of 75.5%—markedly exceeding the error metrics of the other evaluated algorithms (Table 11). This discrepancy likely stems from the algorithm's original calibration using data from turbid inland and estuarine systems, which reduces its effectiveness in the relatively transparent waters of the Arctic.

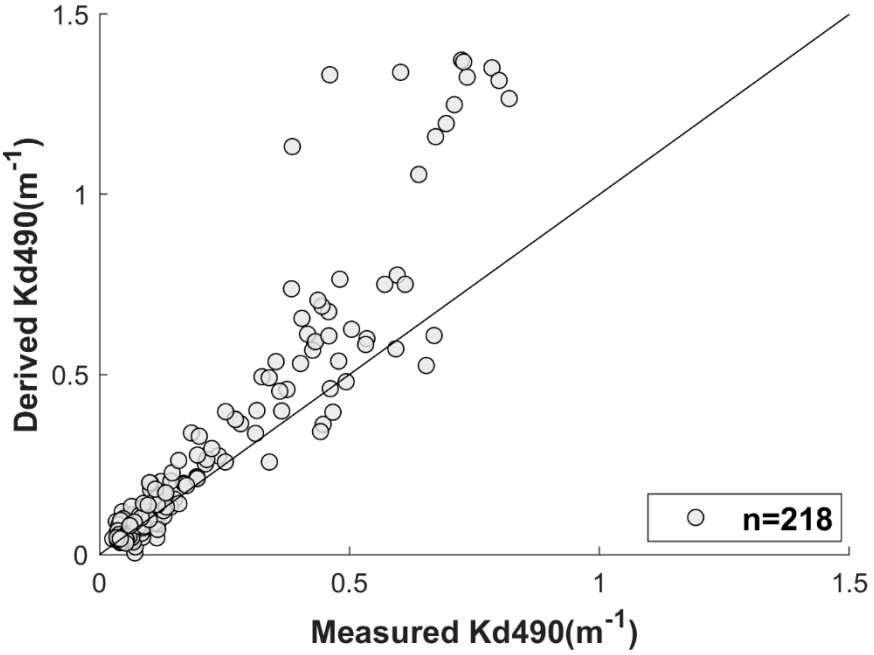


Figure S2: Comparison between measured and algorithm-derived $K_{\mathrm{d}}(490)$ values. Each point represents a matched pair of in-situ and estimated data. The solid line indicates y=x.